WISHED: Wavefront imaging sensor with high resolution and depth ranging

Yicheng Wu*, Fengqiang Li*, Florian Willomitzer, Ashok Veeraraghavan, Oliver Cossairt

Abstract—Phase-retrieval based wavefront sensors have been shown to reconstruct the complex field from an object with a high spatial resolution. Although the reconstructed complex field encodes the depth information of the object, it is impractical to be used as a depth sensor for macroscopic objects, since the unambiguous depth imaging range is limited by the optical wavelength. To improve the depth range of imaging and handle depth discontinuities, we propose a novel three-dimensional sensor by leveraging wavelength diversity and wavefront sensing. Complex fields at two optical wavelengths are recorded, and a synthetic wavelength can be generated by correlating those wavefronts. The proposed system achieves high lateral and depth resolutions. Our experimental prototype shows an unambiguous range of more than 1,000$\times$ larger compared with the optical wavelengths, while the depth precision is up to 9μm for smooth objects and up to 69μm for rough objects. We experimentally demonstrate 3D reconstructions for transparent, translucent, and opaque objects with smooth and rough surfaces.

Index Terms—3D imaging, Wavelength diversity, Wavefront sensing, Phase retrieval

1 Introduction

Optical fields from an object contain information about both albedo and depth. However, intensity-based CCD/CMOS sensors can only record the amplitude of a complex optical field.

In order to reconstruct a complex-valued optical field that contains both amplitude and phase information, wavefront sensors can be used. The Shack-Hartmann wavefront sensor (SHWFS) [1] is the most common wavefront sensor and it relies on a lenslet array. This reduces the spatial resolution of the recovered wavefront to the number of lenses in the array, typically a few tens of thousands.

Recently, a number of high-resolution wavefront sensors (HR-WFS) have been introduced by relying on optical modulation and computational reconstruction. Wang et al. [2] and Horisaki [3] recover megapixel resolution wavefronts using coded apertures. Wu et al. [4] propose a wavefront imaging sensor (a.k.a WISH) with several megapixels resolution by using a programmable spatial light modulator (SLM).

HR-WFS can be used to recover high lateral spatial resolution, but depth information is encoded in phase relative to optical wavelengths, producing an unambiguous depth range in the hundreds of nanometers (one optical wavelength). Phase unwrapping algorithms may help alleviate this issue, but typically fail for objects with discontinuities. *The problem of phase wrapping gets even more severe for optically rough surfaces since it results in a speckle pattern that has random phase distribution (see Fig. 1f)*. The speckle problem manifests for any WFS technique so that none can be used as a general purpose.

The goal of this work is to develop a wavefront sensor capable of measuring the depth of objects with large surface variations (orders of magnitude larger than optical wavelengths) and objects with rough surfaces. Our approach is inspired by interferometry. Optical interferometry is a wavefront sensing technique that uses a reference beam to record the complex field, which suffers from a similar limitation on the unambiguous depth range. To circumvent this limitation, multi-wavelength interferometry is proposed [5], [6], [7]. For example, two wavelengths (λ_1, λ_2) are used to record a complex field, and a complex field with the synthetic wavelength ($\Lambda = \lambda_1 \cdot \lambda_2 / |\lambda_1 - \lambda_2|$) can be then calculated. Since the synthetic wavelength is much larger than optical wavelengths, multi-wavelength interferometry can provide several orders of magnitude improvement in the unambiguous depth range that can be recovered.

In this paper, we leverage two ideas. First, by exploiting computational wavefront sensors (e.g., WISH [4] in this work), we can achieve high lateral resolution wavefront sensing. Second, by exploiting wavelength diversity, we can achieve a large unambiguous depth range in recovery.

We introduce a wavefront imaging sensor with high resolution and depth ranging (WISHED), which allows us to achieve tens of micron lateral resolution and an unambiguous range more than 1,000$\times$ larger than the optical wavelengths. Our WISHED prototype utilizes a tunable laser to provide wavelength diversity and a programmable synthetic wavelength. To reconstruct the depth information, first a wavefront from the object is reconstructed for each wavelength. Then, the difference in phase between these two measured wavefronts is calculated, and the depth is computed relative to the resulting synthetic wavelength. We summarize our contributions as follows.

- We leverage wavelength diversity with wavefront

- * *These two authors contributed equally.*
- *Y. Wu and A. Veeraraghavan are with the Department of Electrical and Computer Engineering, Rice University, Houston, TX 77005 USA.*
- *F. Li and O. Cossairt are with the Department of Computer Science, Northwestern University, Evanston, IL 60208 USA.*
- *F. Willomitzer is with the Department of Electrical and Computer Engineering, Northwestern University, Evanston, IL 60208 USA.*
- *Corresponding authors: A. Veeraraghavan (email: vashok@rice.edu) and O. Cossairt (email: ollie@eecs.northwestern.edu)*

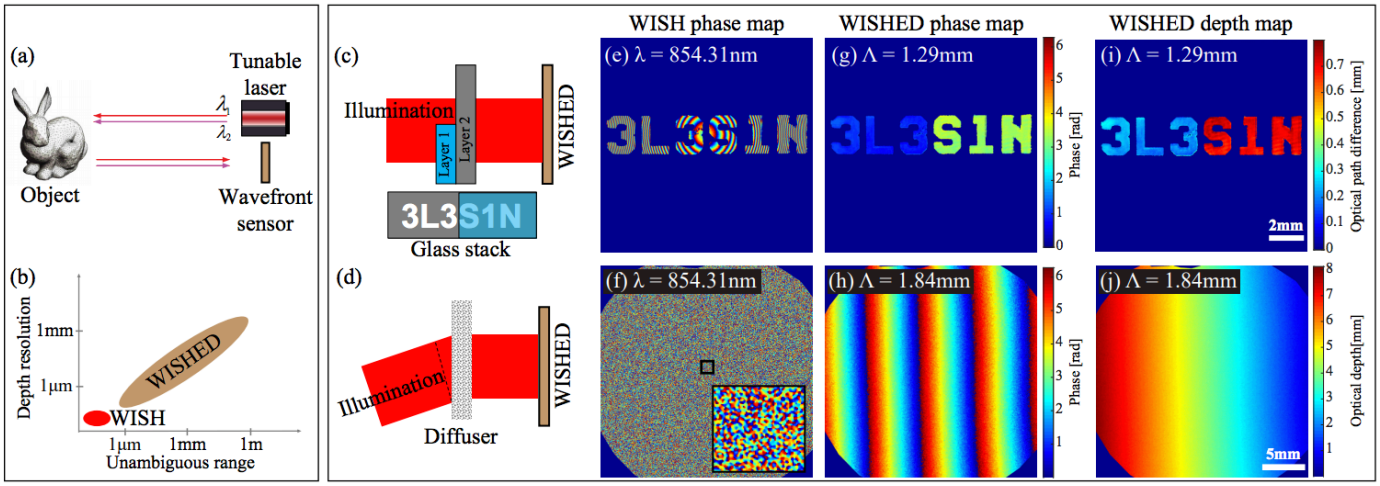

Fig. 1. **Overview of the proposed WISHED system.** (a) The proposed WISHED setup consists of a tunable laser and a wavefront sensor. (b) Comparing to WISH, the proposed WISHED has a much larger unambiguous imaging range with high depth resolution. Our system can work for both optically smooth and rough objects. (c) Experimental setup with two layers of glass slides with letter masks placed in front. The optical path difference between the two layers is about 0.5mm. (d) Experimental setup for recovering a tilted wavefront incident on a diffuser (Thorlabs Grit 220). (e,f) show the recovered phase map from WISH. Since the phase is highly wrapped, and contains discontinuity (e) and speckle (f), the correct optical path difference cannot be recovered. In contrast, the phase map (g,h) from WISHED shows little (h) or no (g) phase wrapping. (i,j) show the unwrapped optical path difference and optical depth, which demonstrates that WISHED is capable of achieving sub-mm depth resolutions.

sensing to propose WISHED as a depth sensor.

- We build a prototype and demonstrate three-dimensional (3D) sensing with high lateral (up to tens of microns) and depth resolutions (up to 9 μm), and large unambiguous range (up to 1.2cm).
- We experimentally demonstrate that WISHED can be used for transparent, translucent, and opaque objects with smooth and rough surfaces.
- The WISHED prototype using a tunable laser provides flexibility in the selection of unambiguous ranges and depth precisions. By combining a multi-wavelength approach and phase unwrapping, we can also achieve a higher dynamic range (the ratio between imaging range and depth resolution), as shown in Fig. 6.

2 Related Work

In this section, we review optical interferometry and phase retrieval algorithms.

2.1 Optical interferometry

In optical interferometry, the detector compares the phase delay in the optical field between sample and reference arms to measure the surface variations of an object. For example, the widely used white light interferometry (WLI) can provide very high depth resolution, and optical coherence tomography is one example of white light interferometry [8]. Focal plane sensors can be used to record a WLI interferogram [9], or a single pixel can be used together with mechanical scanning to record the whole object [10]. Detection can be broadly separated into homodyne and heterodyne techniques. In homodyne detection, the carrier frequencies in two arms are the same. In heterodyne interferometry, the carrier frequencies in two arms are different, which helps with the phase estimation [11]. Single-shot heterodyne interferometry has been proposed with a polarized camera [12]. Kadambi et al. [13] also use heterodyne interferometry to build a GHz time-of-flight imager with micron depth resolution.

Although interferometry with a single wavelength provides extremely high depth resolution, it can not measure objects with rough surfaces since speckles destroy the depth measurement [14]. To measure optically rough objects, multiple phase-wrapped measurements can be made sequentially using different optical wavelengths, then phase unwrapping algorithms can be used to recover the depth of the object [15]. On the other hand, Dändliker et al. [7] propose superheterodyne interferometry (SH) to measure objects with two closely spaced wavelengths simultaneously. Li et al. [16] further demonstrate that SH can be used to measure depth for objects with an optically rough surface, and demonstrate the use of tunable lasers to provide a trade-off between range and resolution. The implementation of SH using a focal plane sensor has also been proposed to remove the need for mechanical scanning [17].

Distinctions between multi-wavelength interferometry and WISHED: Both methods can provide high-resolution wavefront sensing. The main difference is that multi-wavelength interferometry needs a reference arm to coherently interfere with the sample beam. However, this results in several limitations. First, the camera essentially records the phase delay caused by the optical path difference (OPD) between the sample and reference beams. Since these two arms are physically separated, even micrometer level object movement (e.g., due to vibrations) may introduce significant phase delays in these two arms, which totally destroys the measurement. Second, to generate a high contrast interferogram on the sensor plane, the power of the sample and reference beams must be matched. This means that a careful calibration of power matching between object and reference beams needs to be performed. Third, the

phase of the reference must be calibrated so that its effect can be factored out of the recovered wavefront. Moreover, most current SH systems are implemented with single-pixel detectors or low-resolution lock-in sensors, while WISHED can use megapixel CCD/CMOS sensors. This means that the spatial resolution of WISHED is much higher.

2.2 Phase retrieval

Since optical frequencies (e.g., 400THz) are much higher than the frame rate of a focal plane detector or the sampling frequency of a single pixel detector, it is generally only possible to record the amplitude of an optical field, but not the phase information. As mentioned above, interferometry can be used to recover the phase directly with the help of a reference beam. On the other hand, non-linear phase retrieval algorithms can be used to estimate the phase (or the complex field) from only intensity measurements. In general, this reconstruction is an ill-posed problem and it is difficult to guarantee uniqueness in reconstructed results.

The most popular phase retrieval algorithm was introduced by Gerchberg and Saxton (GS) [18], which iteratively imposes sensor-plane and object-plane constraints. Although it is not guaranteed to recover to the true solution, the GS algorithm works well in practice provided sufficiently strong constraints. Researchers have proposed a number of techniques to improve the convergence of the initial GS algorithm. Several methods focus on increasing the number of uncorrelated measurements (stronger constraints), including adding measurements at different propagation planes [19], [20] or with different phase modulations [4], [21]. More sophisticated phase retrieval algorithms have also been introduced using new ideas such as convex relaxations [22], [23], approximate message passing [24], [25] and deep learning [26].

Non-linear phase retrieval algorithms have been a key component for many imaging techniques, such as wavefront sensing [2], [4], [21], [27], Ptychography [28], [29], and Fourier Ptychography [30], [31].

3 Proposed Method

The key idea of our approach is to borrow the wavelength diversity that is often used in interferometry, and leverage with the high-resolution computational wavefront sensing. First, we explain a phase retrieval algorithm to reconstruct the wavefront. Then, we introduce a method for depth estimation with a synthetic wavelength that is several orders of magnitude larger than the optical wavelength.

3.1 Wavefront recovery using phase retreival

We follow the idea proposed by WISH [4], and design a wavefront sensor with an SLM and a CMOS sensor to record the optical field. N uncorrelated random phase patterns $\Phi^i_{SLM}(i = 1 \cdots N)$ are displayed on the SLM to modify the incident wavefront. The corresponding intensity $I^i(i = 1 \cdots N)$ is captured by the sensor at distance z. The relation between the unknown field u_{sensor} that falls on the SLM and the measurement I^i can be represented as

$$I^i = |P_z \Phi^i_{SLM} P_{-z} u_{sensor}|^2 \tag{1}$$

P_z is the propagation operator [32] calculating the field at distance z.

In our system, we first recover the field right before the SLM ($u_{SLM} = P_{-z} u_{sensor}$). Then u_{sensor} be calculated based on numerical propagation. To estimate u_{SLM}, we rewrite Eq. 1 as an optimization form,

$$\hat{u}_{SLM} = \arg\min \sum_i^N \left\| \sqrt{I^i} - |P_z \Phi^i_{SLM} u_{SLM}| \right\| \tag{2}$$

To solve this phase retrieval program, we apply the GS algorithm [18]. The GS algorithm gives accurate results when the phase modulation is random [33]. Here, this requirement is satisfied by projecting random SLM patterns. More measurements lead to better convergence, especially for rough objects. Empirically, we find 16 SLM measurements give us robust reconstruction results in most cases. Our algorithm does not enforce any prior information on the estimated field, which allows it to achieve good results for both optically smooth and rough surfaces.

This iterative algorithm is shown in Algorithm 1. For the initialization, $\hat{u}_{SLM}$ is the average of the fields back-propagated from the sensor plane with captured amplitudes $\sqrt{I^i}$ and zero (or random) phases. During each iteration, $\hat{u}_{SLM}$ is modulated by Φ^i_{SLM} and then propagates to the sensor. On the sensor plane, for each y^i, the amplitude is replaced by the corresponding measurement $\sqrt{I^i}$. Next, these fields are propagated back to the SLM plane, multiplied with the inverted field of the SLM plane, and averaged. The estimation will finally converge with several iterations. After the estimation of the optical field on the SLM plane, we can calculate the optical field on the sensor plane with a forward propagation.

Algorithm 1 Wavefront recovery alogrithm

initialize field $\hat{u}_{SLM} = \sum_i (P_{-z}\sqrt{I^i})/N$
while $\sum_i (y^i - \sqrt{I^i}) > \epsilon$ **do**
  propagate to sensor plane: $y^i = P_z \Phi^i_{SLM} \hat{u}_{SLM}$
  constraint amplitude: $y^i_c = \sqrt{I^i} \angle y^i$
  propagate to SLM plane: $\hat{u}^i_{SLM} = \left(\Phi^i_{SLM}\right)^{-1} P_{-z} y^i_c$
  average the field: $\hat{u}_{SLM} = \sum_i \hat{u}^i_{SLM}/N$
output the field on the sensor $\hat{u}_{sensor} = P_z \hat{u}_{SLM}$

3.2 Depth estimation with multiple wavelengths

The optical field $O_{\lambda_i}(x, y)$ recorded on the sensor plane encodes the surface variation of the object $d(x, y)$ and albedo $a_{\lambda_i}(x, y)$ as:

$$O_{\lambda_i}(x, y) = a_{\lambda_i}(x, y) exp^{\{i2\pi \frac{d(x,y)+\delta d(x,y)}{\lambda_i}\}} \tag{3}$$

where $\delta d(x, y)$ is the roughness of point (x, y) on the object.

For an optically smooth object ($\delta d(x, y)$=0), we can estimate the phase with only one wavelength. However, for macroscopic objects ($d \gg \lambda_i$) with discontinuities, it is challenging to unwrap the phase and convert into depth. On the other hand, for rough surfaces ($\delta d(x, y) \neq$0), it introduces a

speckle pattern that has random phase distribution, which fails the depth measurement.

To decode the depth for objects with discontinuities or rough surfaces, we combine the optical fields with two close wavelengths to estimate the depth information. The phase difference or depth can be calculated by pointwise multiplication between the field of λ_1 and the conjugate field of λ_2.

$$O_{\lambda_1} \odot (O_{\lambda_2})^* = (a_{\lambda_1} exp^{\{i2\pi \frac{d}{\lambda_1}\}}) \odot (a_{\lambda_2} exp^{\{i2\pi \frac{d}{\lambda_2}\}})^* \quad (4)$$

$$d = \angle (O_{\lambda_1} \odot (O_{\lambda_2})^*) \cdot \frac{1}{2\pi} \cdot \frac{\lambda_1 \lambda_2}{|\lambda_1 - \lambda_2|} \quad (5)$$

where λ_1 and λ_2 are the two wavelengths to estimate the depth or phase of the object. Synthetic wavelength is defined as $\Lambda = \frac{\lambda_1 \lambda_2}{|\lambda_1 - \lambda_2|}$. $\odot$ represents the point-wise multiplication, and $()^*$ represents the conjugate of the complex value. The micro surface roughness $\delta d(x, y)$ is far smaller than the macro surface height $d(x, y)$. Therefore, the WISHED reconstructed depth represents the macro surface height of the object.

During the experiment, the values of these two wavelengths are chosen very close (<0.2nm) to produce a large synthetic wavelength Λ (>5mm), which helps measure the surface with large height variation.

3.3 Phase unwrapping

To achieve both high depth resolution and large imaging range, we can utilize two measurements: one with a small synthetic wavelength and the other with a large synthetic wavelength. The small synthetic wavelength provides high depth resolution, but the overall measurement can be wrapped. We can use a depth measurement with a large synthetic wavelength and no phase wrapping as a guide to unwrap measurements with the smaller synthetic wavelength as below [34]:

$$\Phi^2_{uw}(\Lambda_2) = \Phi_w(\Lambda_2) + 2\pi \cdot \mathbf{round}\left(\frac{M \cdot \Phi^1_{uw}(\Lambda_1) - \Phi_w(\Lambda_2)}{2\pi}\right) \quad (6)$$

where M equals to Λ_1/Λ_2. Φ^1_{uw} is the phase measurement of the large synthetic wavelength Λ_1 without wrapping. Φ_w is the wrapped phase measurement using the small synthetic wavelength Λ_2. Φ^2_{uw} is the unwrapped phase that needs to be estimated. Once we estimate Φ^2_{uw}, we can convert it into depth with Eq. 5.

For simple objects such as a planar surface, we can also directly use a fast two-dimensional phase-unwrapping algorithm by adding integer times of 2π at the phase jump regions [35] to unwrap phase measurements with small synthetic wavelengths.

4 Simulation

In this section, we show simulation results based on the proposed WISHED. Without loss of generality, we demonstrate simulations estimating the depth of an opaque object with rough surfaces in reflective mode.

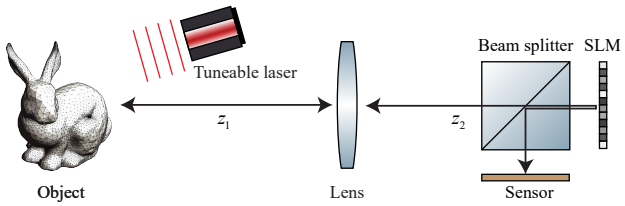

Fig. 2. **Simulation setup.** The laser beam with a tuneable wavelength is first scattered by the object and then collected by the lens. A wavefront sensor containing an SLM and a CMOS imager is used to record the complex field.

4.1 Simulation settings

The setup for our simulation is shown in Fig. 2. We pick the Stanford Bunny [36] as our object. To model the rough surface, we add a height variation following a Gaussian distribution on the top of the height map of the bunny. The final height map is $h = h_{bunny} + \mathcal{N}(0, 1\mu\text{m})$. The maximum height difference for the bunny is 10mm.

The two wavelengths used here are $\lambda_a = 854.985$nm and $\lambda_b = 855.015$nm. The synthetic wavelength is $\Lambda = 24.4$mm. The bunny is illuminated by the laser beam with each wavelength sequentially. The scattering light is collected by a 15-mm-diameter lens at distance $z_1 = 600$mm with 85.7mm focal length. The light is focused at $z_2 = 100$mm away from the lens. Since the sensor is on the conjugate plane of the object plane, u_{sensor} can be directly calculated based on Fourier Optics theory [32],

$$u_{sensor} = \mathcal{Q}\Big[\frac{z_1 + z_2}{z_2^2}\Big]\mathcal{V}\Big[-\frac{z_1}{z_2}\Big]u_{obj} \quad (7)$$

$\mathcal{Q}$ represents multiplication by a quadratic-phase exponential and $\mathcal{V}$ represents scaling by a constant. Based on this equation, once we recover u_{sensor}, u_{obj} can be calculated accordingly. Then the depth map can be recovered based on Eq. 5.

4.2 Depth estimation

In the simulation, we generate 16 random SLM patterns and calculate the corresponding intensity images on the sensor. To mimic noise in the real experiment, we add a Gaussian noise with $\sigma = 0.2$ into the measurement. Fig. 3 shows several simulated sensor measurements for two wavelengths.

Based on the phase retrieval algorithm mentioned in Sec. 3.1, the reconstructed field on the sensor is shown in Fig. 4(a). Because of the roughness of the bunny, the amplitude contains speckle patterns, and the phase looks random. Based on the Eq. 5, we recover the heightmap of the object. Due to the slight difference of the Airy disk diameters between two wavelengths, the recovered depth map contains artifacts near the boundary of the speckle pattern. To reduce such artifacts, a Gaussian kernel with the size of the averaged Airy disk is applied to smooth the depth map. The result is shown in Fig. 4(b), which is quite close to the ground truth (RMSE = 85μm for Λ = 24.4mm). Note that the surface roughness (1μm) is much smaller than the RMSE (85μm). Therefore, the recovered macroscopic heightmap is not affected by the surface roughness.

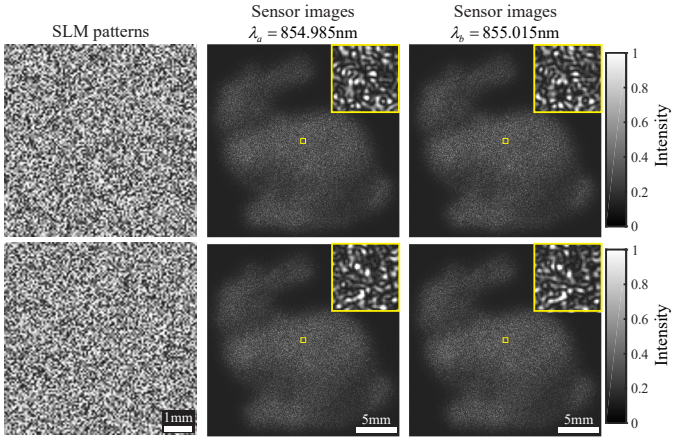

Fig. 3. **Simulated sensor measurements with different SLM patterns and optical wavelengths.** For each SLM pattern, the speckle patterns are close for two similar wavelengths. For different SLM patterns, the speckle patterns are totally distinct to make sure these measurements are uncorrelated.

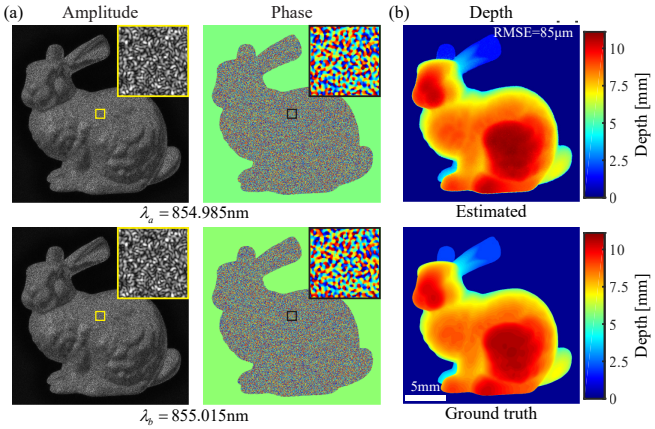

Fig. 4. **Simulation reconstruction.** (a) Recovered object fields for two wavelengths. (b) Comparison between ground truth and WISHED estimated depth using a synthetic wavelength of 24.4mm (RMSE = 85μm).

5 Experimental Results

In this section, we report experimental measurements using our prototype WISHED sensor for transparent, translucent, and opaque objects. The optical configuration is identical to the one used for simulations, as illustrated in Fig. 2. A tunable laser (Toptica DLC pro850) with the center wavelength of 850nm is used as the light source. We image the object with multiple wavelengths by tuning the frequency of the laser emission. The laser emission is collimated and then illuminates the object either in transmissive or reflective mode. A linear polarizer is used to match the polarization of the SLM (HOLOEYE LETO, 1920 $\times$ 1080 resolution, 6.4μm pitch size) since SLM is only sensitive to a specific polarization direction. The focusing lens (Thorlabs AC508-075-B-ML) has a focal length of 75mm and is placed about 50cm away from the object. A 25.4-mm beam splitter is inserted between the SLM and the sensor to guide the field into the sensor since the SLM operates in the reflective mode. The distance between the SLM and the sensor is 25 mm. The sensor is a 10-bit Basler Ace camera (acA4024-29um) equipped with a Sony IMX-226 CMOS sensor (1.85 μm pixel pitch, 4024 $\times$ 3036 resolution).

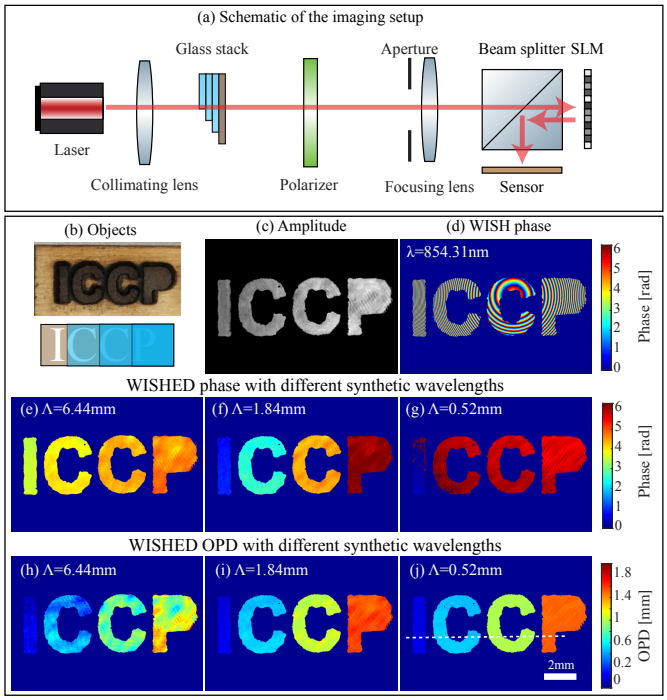

Fig. 5. **Experiment on optical smooth objects in transmissive mode.** (a) Setup illustration. (b) The object: a letter mask with a glass stack in front. (c) Amplitude measurement. (d) WISH reconstruction: phase maps with one optical wavelength. (e-g) WISHED reconstruction: phase maps with different synthetic wavelengths. (h-j) OPD with different synthetic wavelengths. Smaller synthetic wavelength provides higher depth precision.

5.1 Transmissive based 3D imaging

To verify the optimal performance and depth resolution with the prototype, we first image different transmissive objects with optically smooth and rough surfaces.

5.1.1 *Imaging an optically smooth planar object*

As shown in Fig. 5(a), the beam is collimated and then illuminates the object – a letter mask with a glass plate stack in front as shown in Fig. 5(b). There are zero, one, two, and three glass plates on top of the letter 'I', 'C', 'C', and 'P', respectively. The surface of the glass plates is optically smooth, and each glass plate introduces an optical path difference of 0.5mm. 16 random SLM patterns are used to modulate the optical field.

Since the surface of the glass plates is smooth, there is no speckle pattern observed as shown in Fig. 5(c). We image the object with an optical wavelength of 854.31nm, 854.43nm, 854.71nm, and 855.73nm, which leads to six different synthetic wavelengths. Here, we show three examples in Fig. 5, corresponding to the synthetic wavelength of 6.44mm, 1.84mm, and 0.52mm. The phase and depth values are estimated with the method described in Sec. 3.2.

As we can see, WISH measurement with one wavelength has severe phase wrapping as shown in Fig. 5(d). It is very challenging to recover the overall phase of the glass stack if we do not know the discontinuities ahead. On the

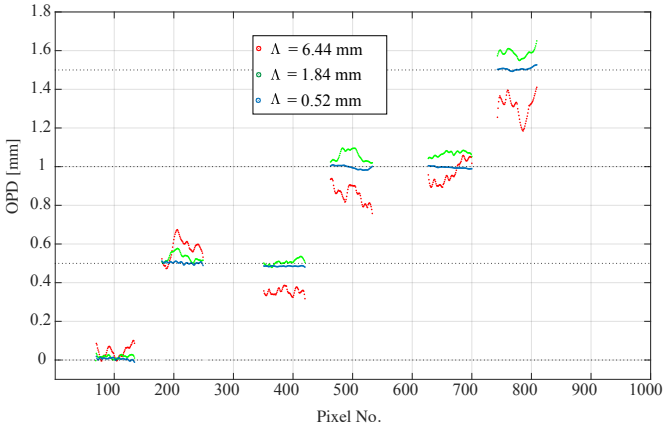

Fig. 6. **OPD profile along one line on the plate stack as shown in Fig 5(h-j).** The x-axis marks the different pixels along the line, and y axis is the OPD. Note: each glass plate introduces an OPD of 0.5mm. The RMSEs of this OPD profile for the synthetic wavelengths of 6.44mm, 1.84mm and 0.52mm are 130μm, 56μm and 9μm.

other hand, WISHED with the larger synthetic wavelengths produces an unambiguous depth range significantly greater than the optical wavelengths, and we can clearly separate these four letters, which have different phases as shown in Fig. 5(e,f). Since the total optical depth of the glass stack is larger than the synthetic wavelength of 0.52mm, we observe phase wrapping in Fig. 5(g). We use the phase unwrapping algorithm of Eq. 6 and the measurement of the synthetic wavelength of 1.84mm as a guide to unwrap. The unwrapped phase of Fig. 5(g) is then converted into depth as shown in Fig. 5(j).

The smaller synthetic wavelength provides better depth resolution as shown in Fig. 5(j) compared to the larger synthetic wavelength shown in Fig. 5(h, i). The same phenomena can be observed in an optical depth profile along a line cut (marked as a dashed line in Fig. 5j) through the glass plate stack as shown in Fig. 6. We further quantify the root mean square errors (RMSE) for the optical depth profile as shown in Fig. 6. We define RMSE as the standard deviation away from the assumed step heights. *The RMSEs for the synthetic wavelengths of 6.44mm, 1.84mm, and 0.52mm are 130μm, 56μm and 9μm*, which demonstrates the very high depth precision of the prototype. The observation of measurements with different synthetic wavelengths also aligns with our intuitive expectation that a smaller wavelength provides finer depth resolution given the same to noise ratio (SNR) in the sensor. Since our prototype is built with a tunable source, it provides a trade-off for different applications requiring different imaging ranges and depth resolutions.

5.1.2 Imaging an optically rough object

We then increase the complexity of the experiment by adding a diffuser behind the glass stack to emulate an optically rough surface as shown in Fig. 7(a). If we look at the images recorded by the sensor without SLM modulation, the speckle pattern is clearly observed as shown in Fig. 7(b,c). Two different wavelengths of 854.31nm and 854.48nm are used, which produces a synthetic wavelength of 4.3mm. The speckle pattern with different wavelengths is

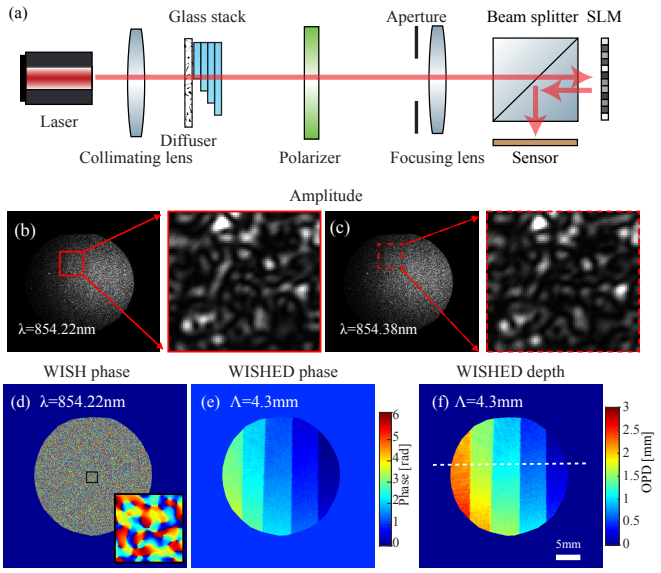

Fig. 7. **Experiment on optical rough objects in transmissive mode.** (a) Setup illustration. (b,c) Amplitude measurement (no SLM modulation) with two close wavelengths 854.22nm (b) and 854.38nm (c). These two speckle patterns are similar since their wavelengths are close. (d) phase map from WISH reconstruction. The 3D information is totally lost due to the speckle pattern. (e) phase map from WISHED reconstruction. The synthetic wavelength is 4.3mm. (f) Estimated OPD, where glass layers are clearly visualized.

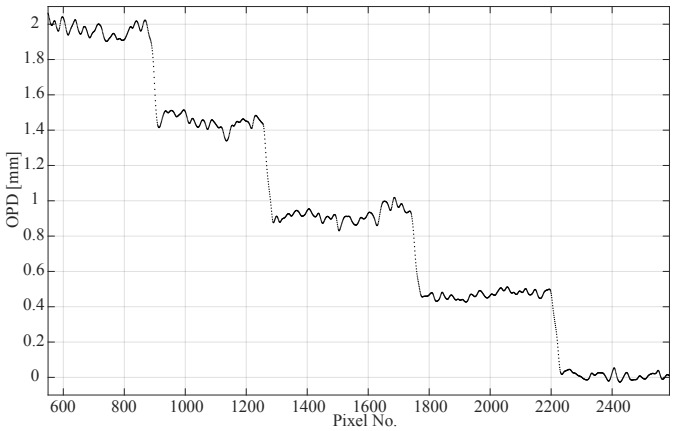

Fig. 8. **OPD profile along one line on the plate stack as shown in Fig. 7(f).** The x-axis marks the different points along the line, and y axis is the OPD value. Note: each glass plate introduces an OPD of 0.5mm. The RMSE in optical depth for the measurement is 69μm.

slightly different. Although the speckle pattern is present, we can still reconstruct the optical depth, which we can convert into a true optical depth map given knowledge of the index of refraction of the transparent object (in this case n=1.5), as shown in Fig. 7. Each glass plate introduces an optical path difference of 0.5mm. The glass plates are clearly separated according to their thickness. A line profile is also plotted across these different glass plates as shown in Fig. 8, demonstrating that we can still achieve a high depth resolution despite the presence of speckle. We quantify the RMSE for the optical depth along with this line profile as 69 μm.

In Fig. 6 and Fig. 8, we did not obtain a ground truth

measurement of glass thickness (or OPD), but rather assume a 'ground truth', following the manufacturing specifications - that each glass plate introduces an OPD of 0.5mm. Therefore, in our assumed ground truth, the steps for the glass plate in Fig. 6 are 0mm, 0.5mm, 1mm, 1,5mm. In Fig. 8, they are 0mm, 0.5mm, 1mm, 1.5mm, 2mm. Our assumed ground truth may have small errors due to manufacturing tolerances.

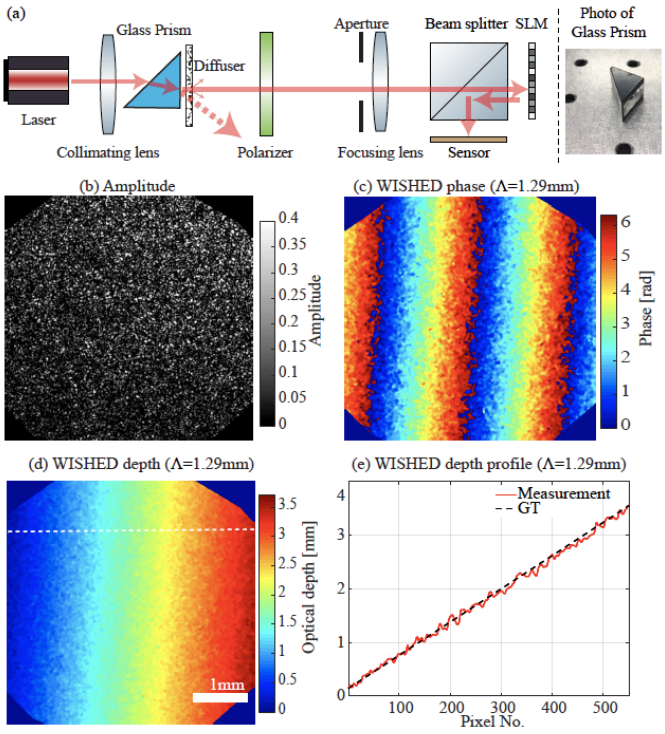

Fig. 9. **Experiment on a transparent object with complex geometry.** (a) Experimental setup for imaging the glass prism. A diffuser is used for scattering the light into the sensor. (b) Amplitude recorded on the sensor plane with one wavelength. (c) The wrapped phase measured with a synthetic wavelength of 1.29mm. (d) The depth converted from the unwrapped phase. (e) A line profile across the object. The RMSE for optical depth along this line profile is 61μm

5.1.3 Imaging a transparent object with complex geometry

Measuring the OPD of a transparent object with complex geometry (contain heavy refractive phenomena) is a challenging problem. The reason is that the light illuminated on the object is redirected due to the refraction on the surface, which means that light from some regions of the object may not reach the sensor. As a result, it is impossible to measure OPD for these regions.

Our WISHED system can offer a new direction to tackle this problem. The key idea is to insert a diffuser right after (or before) the object. On the one hand, light from all regions of the object gets scattered by the diffuser, which ensures that the sensor can gather light from the entire object. On the other hand, the overall OPD from the object is recovered with WISHED since the synthetic wavelength is much larger than the height variation (similar to the roughness of opaque surfaces) introduced by the diffuser.

As shown in Fig. 9(a), we image a triangular prism as a proof-of-concept. The beam is not directed to the detector due to the refraction, and a diffuser (Thorlabs 220 Grit) is used to scatter light to the detector. There are speckles in the sensed image as shown in Fig. 9(b). Wavelengths of 854.31nm and 854.88nm are used, which corresponds to a synthetic wavelength of 1.29mm. The phase with the synthetic wavelength is shown in Fig. 9(c), and a phase unwrapping algorithm [11] is used to unwrap the phase and convert to optical path difference as shown in Fig. 9(d). A line profile across the optical depth map is shown in Fig. 9(e), which demonstrates a 61μm depth resolution.

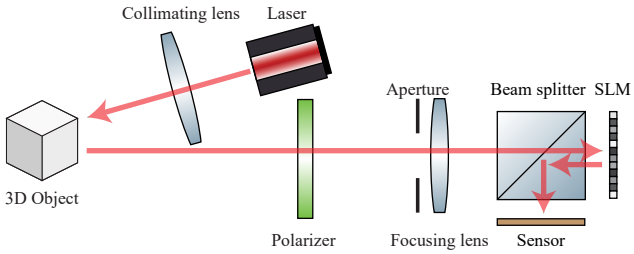

Fig. 10. **Experiment schematics for reflective 3D objects.** The object is illuminated by the tunable laser. And the scattering light is collected by a focusing lens to our wavefront sensors.

5.2 Reflective based 3D imaging

Most macroscopic objects are not transparent, so we test our proposed method to image some non-transparent objects as shown in Fig. 10. We note that for reflective geometries, the depth calculated is physical (not optical) since light is assumed to propagate through air, and reflect at the surface boundary (subsurface scattering is discussed in Sec. 6).

We first image a metal plate stack including two planar metal plates with rough surfaces. The two metal plates are separated by 6mm. 24 random patterns are displayed on the SLM to modulate the incoming optical field for each wavelength. We image with four different wavelengths (854.22nm, 854.27nm, 854.38nm, and 854.49nm), which gives six different synthetic wavelengths. Since multiple measurements are made, we can use the measurement with the large synthetic wavelength as a guide to unwrap the depth measured with small synthetic wavelengths. In Fig. 11, we show the recovered depth map with a large synthetic wavelength of 13.2mm and the unwrapped depth map with a small synthetic wavelength of 2.6mm. Both these results provide similar measurements showing that the height difference for the left and right regions is about 6mm. For a smaller synthetic wavelength, the measurement is less noisy with a smaller RMSE, as long as the phase unwrapping is correct.

We also image a penny as shown in Fig. 12(b). 40 random patterns are displayed on the SLM to modulate the incoming optical field for each wavelength. The stand-off distance is about 0.5 meters between the object and the sensor. Two wavelengths of 854.22nm and 854.49nm are used to estimate the depth map, which corresponds to a synthetic wavelength of 2.63mm. The depth map estimated with the proposed method is shown in Fig. 12(c) where we can observe many details of the coin surface. For example, the 'shield' layer is clearly observed. Even the letter 'C' in

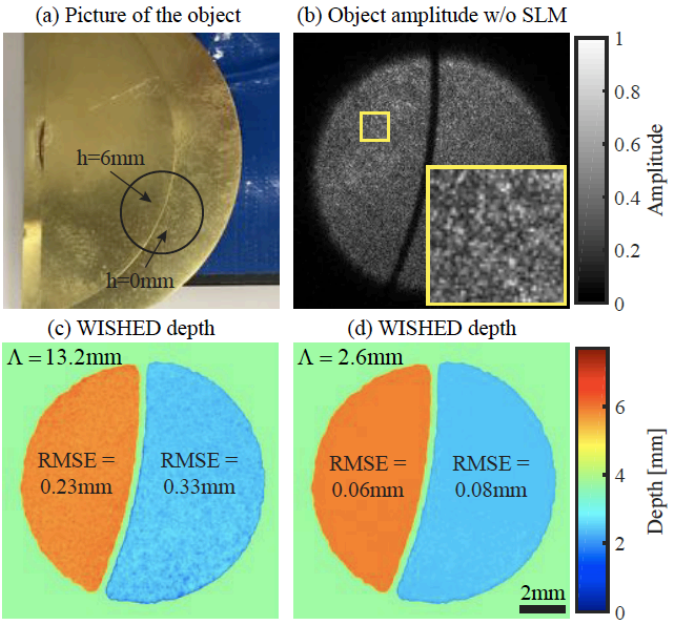

Fig. 11. **Experiment on a metal plate stack in reflective mode.** Speckles are observed in (b) due to the surface roughness of the metal plates. The results (c,d) show the depth map from two synthetic wavelengths. The estimation from the smaller synthetic wavelength has less height variation.

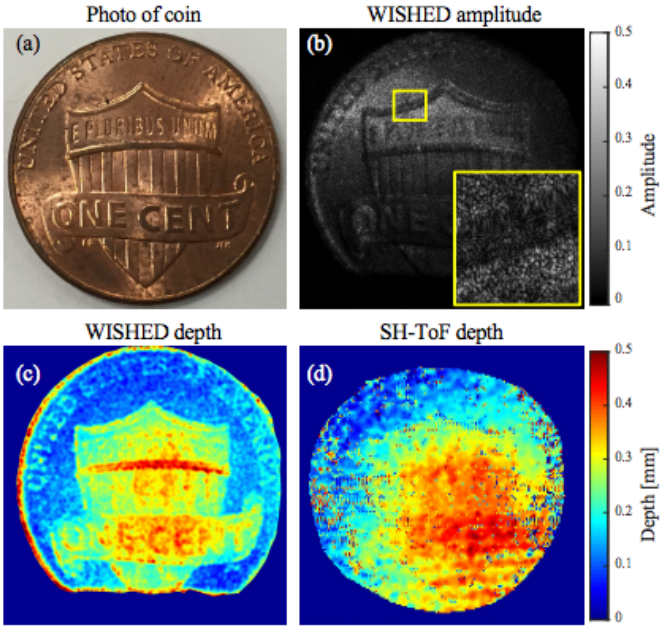

Fig. 12. **Experimental results of the penny.** (a) Picture of the penny to measure. (b) Captured amplitude without the SLM modulation. The speckle pattern is observed due to the surface roughness. (c) Recovered depth map using the proposed WISHED method. (d) Recovered depth map using the SH-ToF with a lock-in camera.

'CENT' is recognized from the depth map. The thickness of the shield is a couple of hundreds of micrometers. According to the result in the metal plate stack (Fig. 11), the RMSE is about 60-80μm. We expect the RMSE for the penny is in a similar range since we use the same synthetic wavelength for both experiments, and the penny has a similar rough appearance to the metal plate. In Fig. 12(c), we can see letters 'UNITED' separately from the background, corresponding to a depth difference of about 100μm. The image shown in Fig. 12(c) has 2100 $\times$ 2100 pixels. We provide an experimental comparison using the SH-ToF technique [16] using a lock-in camera [37] with a synthetic wavelength of 1.73mm as shown in Fig. 12(d) (155$\times$155 pixels). The stand-off distance is the same as the measurement using WISHED. Although the depth precision is comparable to our WISHED prototype, lateral spatial resolution is significantly reduced due to the low resolution of the lock-in focal plane array.

6 Discussion

Effect of subjective speckle size: We experimentally verify the effect of subjective speckle size as shown in Fig. 13(a). The setup is exactly the same with that in Sec. 5.1.2, with the only difference being that aperture size is increased by three times so that several subjective speckles are averaged at each pixel (approximately two speckles per pixel in this experiment). In contrast, all the previous experiments used a smaller aperture size so that subjective speckles were larger than a pixel. The wrapped phase image for each wavelength is reconstructed separately, and the synthetic wavelength phase is generated from these two wrapped phase images as shown in Fig. 13(b).

As we can see, there are errors in the reconstruction using the synthetic wavelength. Moreover, the reconstruction of measurements with smaller subjective speckle sizes takes much longer to converge. This is most likely due to the fact that the phase retrieval algorithm does not sufficiently model the effects of speckle averaging, which can severely reduce speckle contrast and generally make the phase retrieval problem much more difficult to solve robustly.

The size of the speckles depends on the aperture of the imaging system:

$$\Delta_{speckle} = \lambda / NA \tag{8}$$

where λ is the wavelength of the illumination and NA is the numerical aperture of the objective lens. To avoid the averaging of speckles on the sensor plane, the pixel size should be smaller than the subjective speckle size. Therefore, the aperture of the system is recommended to satisfy the condition shown below

$$NA < \lambda / p \tag{9}$$

where p is the pixel size.

Limitation of the prototype: A reflective SLM is used in our current prototype, and a one-inch beam splitter has to be inserted between the SLM and the sensor. This setup limits the field of view (FOV) of the current prototype. In order to increase the FOV and image large objects, a transmissive SLM can be used with a small focal length objective lens.

In our current prototype, both the acquisition speed and reconstruction are not optimized for moving objects in real-time. We believe this can be addressed based on the recent development in deep learning. For the current acquisition, multiple measurements with different SLM patterns are required to reconstruct the wavefront. We can constraint our reconstruction space by enforcing prior learned from a network [38], which can reduce the number of measurements

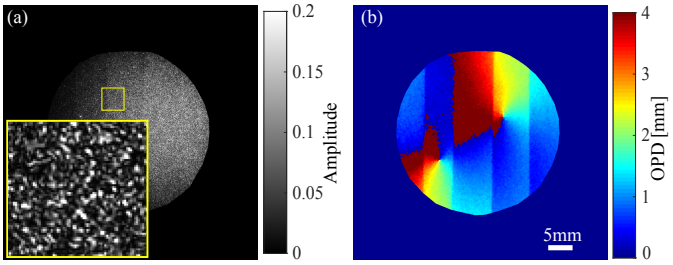

Fig. 13. **Failure case with WISHED:** Imaging the glass stack with a diffuser as shown in Fig. 7 with speckles averaged on the sensor plane. (a) Amplitude with speckles averaged on the sensor plane. (b) Reconstructed depth profile with the same synthetic wavelength using the proposed method.

dramatically. For the reconstruction, our current iterative algorithm can be unrolled to be a neural network [26], which outputs the reconstructed field much faster.

Limitation of this principle: As we mentioned previously, a tunable source is used to produce different synthetic wavelengths. Small synthetic wavelengths provide very high depth resolution. However, if multiple scattering is present (i.e., subsurface scattering, surface inter-reflections) [39], the optical path length recovered using WISHED (or any other interferometry technique) will not correspond directly to surface height. Furthermore, even in the absence of multi-path interference, the upper bound performance of the proposed method is surface roughness. In other words, the depth resolution can not be less than the peak-to-valley surface variation with the lateral resolution of the imager.

For smooth objects, the lateral resolution is limited by the Airy disk size and the sensor pixel size. For rough objects, since we need to resolve the subjective speckle size in the sensor plane (as discussed previously), the lateral resolution of this method is limited by the subjective speckle size.

7 Conclusion

In this paper, we propose a high lateral and depth resolution sensor with a large depth range, termed WISHED. We demonstrate that the proposed method is able to measure accurate 3D profiles for both optically smooth and rough objects in both transmissive and reflective geometries. We believe our system can be developed into a robust 3D imaging technique for high precision applications in metrology and biomedical imaging. The proposed system also has the potential for some extreme imaging scenarios such as non-line-of-sight imaging and 3D imaging of complex transparent objects.

Acknowledgments

This work is supported by DARPA Reveal (HR0011-16-C-0028), NSF CAREER (IIS-1453192, IIS-1652633), NSF Expeditions (CCF-1730574), and ERC PATHS-UP (EEC-1648451). We also thank Prasanna Rangarajan and Muralidhar Madabhushi for assistance on capturing the depth map of the coin with the lock-in sensor.

References

[1] B. C. Platt and R. Shack, "History and principles of shack-hartmann wavefront sensing," *Journal of refractive surgery*, vol. 17, no. 5, pp. S573–S577, 2001.

[2] C. Wang, X. Dun, Q. Fu, and W. Heidrich, "Ultra-high resolution coded wavefront sensor," *Optics express*, vol. 25, no. 12, pp. 13 736–13 746, 2017.

[3] R. Horisaki, "Single-shot phase imaging with coded diffraction and its applications," in *3D Image Acquisition and Display: Technology, Perception and Applications*. Optical Society of America, 2018, pp. 3M3G–1.

[4] Y. Wu, M. K. Sharma, and A. Veeraraghavan, "Wish: wavefront imaging sensor with high resolution," *Light: Science & Applications*, vol. 8, no. 1, p. 44, 2019.

[5] Y.-Y. Cheng and J. C. Wyant, "Two-wavelength phase shifting interferometry," *Appl. Opt.*, vol. 23, no. 24, pp. 4539–4543, 1984.

[6] A. Fercher, H. Z. Hu, and U. Vry, "Rough surface interferometry with a two-wavelength heterodyne speckle interferometer," *Applied optics*, vol. 24, no. 14, pp. 2181–2188, 1985.

[7] R. Dändliker, R. Thalmann, and D. Prongué, "Two-wavelength laser interferometry using superheterodyne detection," *Opt. Lett.*, vol. 13, no. 5, pp. 339–341, 1988.

[8] D. Huang, E. A. Swanson, C. P. Lin, J. S. Schuman, W. G. Stinson, W. Chang, M. R. Hee, T. Flotte, K. Gregory, C. A. Puliafito *et al.*, "Optical coherence tomography," *science*, vol. 254, no. 5035, pp. 1178–1181, 1991.

[9] A. Nahas, M. Bauer, S. Roux, and A. C. Boccara, "3d static elastography at the micrometer scale using full field oct," *Biomedical optics express*, vol. 4, no. 10, pp. 2138–2149, 2013.

[10] F. Li, J. Yablon, A. Velten, M. Gupta, and O. Cossairt, "High-depth-resolution range imaging with multiple-wavelength superheterodyne interferometry using 1550-nm lasers," *Applied optics*, vol. 56, no. 31, pp. H51–H56, 2017.

[11] N. Massie, R. Nelson, and S. Holly, "High-performance real-time heterodyne interferometry," *Applied Optics*, vol. 18, no. 11, pp. 1797–1803, 1979.

[12] T. Maeda, A. Kadambi, Y. Y. Schechner, and R. Raskar, "Dynamic heterodyne interferometry," in *2018 IEEE International Conference on Computational Photography (ICCP)*. IEEE, 2018, pp. 1–11.

[13] A. Kadambi and R. Raskar, "Rethinking machine vision time of flight with ghz heterodyning," *IEEE Access*, vol. 5, pp. 26 211–26 223, 2017.

[14] J. W. Goodman, *Speckle phenomena in optics: theory and applications*. Roberts and Company Publishers, 2007.

[15] Y.-Y. Cheng and J. C. Wyant, "Multiple-wavelength phase-shifting interferometry," *Appl. Opt.*, vol. 24, no. 6, pp. 804–807, 1985.

[16] F. Li, F. Willomitzer, P. Rangarajan, M. Gupta, A. Velten, and O. Cossairt, "Sh-tof: Micro resolution time-of-flight imaging with superheterodyne interferometry," in *2018 IEEE International Conference on Computational Photography (ICCP)*. IEEE, 2018, pp. 1–10.

[17] F. Li, F. Willomitzer, P. Rangarajan, and O. Cossairt, "Mega-pixel time-of-flight imager with ghz modulation frequencies," in *Computational Optical Sensing and Imaging*. Optical Society of America, 2019, pp. CTh2A–2.

[18] R. W. Gerchberg, "A practical algorithm for the determination of phase from image and diffraction plane pictures," *Optik*, vol. 35, pp. 237–246, 1972.

[19] N. Streibl, "Phase imaging by the transport equation of intensity," *Optics communications*, vol. 49, no. 1, pp. 6–10, 1984.

[20] M. Soto and E. Acosta, "Improved phase imaging from intensity measurements in multiple planes," *Applied optics*, vol. 46, no. 33, pp. 7978–7981, 2007.

[21] F. Zhang, G. Pedrini, and W. Osten, "Phase retrieval of arbitrary complex-valued fields through aperture-plane modulation," *Physical Review A*, vol. 75, no. 4, p. 043805, 2007.

[22] E. J. Candes, T. Strohmer, and V. Voroninski, "Phaselift: Exact and stable signal recovery from magnitude measurements via convex programming," *Communications on Pure and Applied Mathematics*, vol. 66, no. 8, pp. 1241–1274, 2013.

[23] E. J. Candes, X. Li, and M. Soltanolkotabi, "Phase retrieval from coded diffraction patterns," *Applied and Computational Harmonic Analysis*, vol. 39, no. 2, pp. 277–299, 2015.

[24] P. Schniter and S. Rangan, "Compressive phase retrieval via generalized approximate message passing," *IEEE Transactions on Signal Processing*, vol. 63, no. 4, pp. 1043–1055, 2014.

[25] C. A. Metzler, M. K. Sharma, S. Nagesh, R. G. Baraniuk, O. Cossairt, and A. Veeraraghavan, "Coherent inverse scattering via transmission matrices: Efficient phase retrieval algorithms and a public dataset," in *2017 IEEE International Conference on Computational Photography (ICCP)*. IEEE, 2017, pp. 1–16.
[26] C. A. Metzler, P. Schniter, A. Veeraraghavan, and R. G. Baraniuk, "prdeep: Robust phase retrieval with a flexible deep network," *arXiv preprint arXiv:1803.00212*, 2018.
[27] V. Katkovnik, I. Shevkunov, N. V. Petrov, and K. Egiazarian, "Computational super-resolution phase retrieval from multiple phase-coded diffraction patterns: simulation study and experiments," *Optica*, vol. 4, no. 7, pp. 786–794, 2017.
[28] F. Pfeiffer, "X-ray ptychography," *Nature Photonics*, vol. 12, no. 1, pp. 9–17, 2018.
[29] J. M. Rodenburg, "Ptychography and related diffractive imaging methods," *Advances in imaging and electron physics*, vol. 150, pp. 87–184, 2008.
[30] G. Zheng, R. Horstmeyer, and C. Yang, "Wide-field, high-resolution fourier ptychographic microscopy," *Nature photonics*, vol. 7, no. 9, p. 739, 2013.
[31] J. Holloway, Y. Wu, M. K. Sharma, O. Cossairt, and A. Veeraraghavan, "Savi: Synthetic apertures for long-range, subdiffraction-limited visible imaging using fourier ptychography," *Science advances*, vol. 3, no. 4, p. e1602564, 2017.
[32] J. W. Goodman, *Introduction to Fourier optics*. Roberts and Company Publishers, 2005.
[33] A. Fannjiang, "Absolute uniqueness of phase retrieval with random illumination," *Inverse Problems*, vol. 28, no. 7, p. 075008, 2012.
[34] W. Xu, E. C. Chang, L. K. Kwoh, H. Lim, W. Cheng, and A. Heng, "Phase-unwrapping of sar interferogram with multi-frequency or multi-baseline," in *Proceedings of IGARSS'94-1994 IEEE International Geoscience and Remote Sensing Symposium*, vol. 2. IEEE, 1994, pp. 730–732.
[35] M. A. Herráez, D. R. Burton, M. J. Lalor, and M. A. Gdeisat, "Fast two-dimensional phase-unwrapping algorithm based on sorting by reliability following a noncontinuous path," *Applied optics*, vol. 41, no. 35, pp. 7437–7444, 2002.
[36] G. Turk and M. Levoy, "Zippered polygon meshes from range images," in *Proceedings of the 21st annual conference on Computer graphics and interactive techniques*. ACM, 1994, pp. 311–318.
[37] H. C3, "[Heliotis], 2019," *Retrieved from https://www.heliotis.ch/html/lockInCameraC3.htm*.
[38] D. Ulyanov, A. Vedaldi, and V. Lempitsky, "Deep image prior," in *Proceedings of the IEEE Conference on Computer Vision and Pattern Recognition*, 2018, pp. 9446–9454.
[39] Q. Li and F. Chiang, "Three-dimensional dimension of laser speckle," *Applied optics*, vol. 31, no. 29, pp. 6287–6291, 1992.

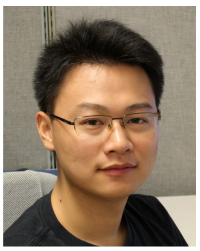

Yicheng Wu is a Ph.D. candidate at Rice University. He is working under the guidance of Ashok Veeraraghavan in the Department of Electrical and Computer Engineering. His current interests are computational imaging, computer vision, and deep learning. Specifically, he jointly designs novel imaging systems and advanced machine learning algorithms for scientific or photographic applications. Previously, he earned his B.S. degree in Physics from Beijing Normal University.

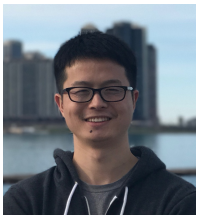

Fengqiang Li is a PhD candidate in Computer Science at Northwestern University. He is working with Prof. Oliver Cossairt in Computational Photography Lab on computational photography and computer vision. Previously, he received his M.S in Electrical Engineering from Lehigh University and B.S in Optoelectronic Information Engineering from Huazhong University of Science and Technology.

Florian Willomitzer is a Research Assistant Professor in the Computational Photography Lab at Northwestern University, IL. Florian graduated from the University of Erlangen-Nuremberg, Germany, where investigated physical and information theoretical limits of optical 3D-sensing and implemented sensors that operate close to these limits. At Northwestern University, Florian develops novel methods to image hidden objects through scattering media or around corners. Moreover, his research is focused on high-resolution holographic displays, the implementation of high-precision metrology methods in low-cost mobile handheld devices, and novel techniques to overcome traditional resolution limitations and dynamic range restrictions in 3D and 2D imaging.

Ashok Veeraraghavan received the bachelor's degree in electrical engineering from the Indian Institute of Technology, Madras, Chennai, India, in 2002 and the M.S. and Ph.D. degrees from the Department of Electrical and Computer Engineering, University of Maryland, College Park, MD, USA, in 2004 and 2008, respectively. He is currently an Associate Professor of Electrical and Computer Engineering, Rice University, Houston, TX, USA. Before joining Rice University, he spent three years as a Research Scientist at Mitsubishi Electric Research Labs, Cambridge, MA, USA. His research interests are broadly in the areas of computational imaging, computer vision, machine learning, and robotics. Dr. Veeraraghavan's thesis received the Doctoral Dissertation Award from the Department of Electrical and Computer Engineering at the University of Maryland. He is the recipient of the National Science Foundation CAREER Award in 2017. At Rice University, he directs the Computational Imaging and Vision Lab.

Oliver Cossairt is Associate Professor in the Computer Science (CS) and Electrical and Computer Engineering (ECE) departments at Northwestern University. Prof. Cossairt is director of the Computational Photography Laboratory (CPL) at Northwestern University (compphotolab.northwestern.edu), whose research consists of a diverse portfolio, ranging in topics from optics/photonics, computer graphics, computer vision, machine learning and image processing. The general goal of CPL is to develop imaging hardware and algorithms that can be applied across a broad range of physical scales, from nanometer to astronomical. This includes active projects on 3D nano-tomography (10^{-9}m), computational microscopy (10^{-6}m), cultural heritage imaging analysis of paintings (10^{-3}m), structured light and ToF 3D-scanning of macroscopic scenes (1m), descattering through fog for remote sensing (10^{3}m), and coded aperture imaging for astronomy (10^{6}m). Prof. Cossairt has garnered funding from numerous corporate sponsorships (Google, Rambus, Samsung, Omron, Oculus/Facebook, Zoloz/Alibaba) and federal funding agencies (ONR, NIH, DOE, DARPA, IARPA, NSF CAREER Award).